Study of HD 169392A observed by CoRoT and HARPS

S. Mathur, H. Bruntt, C. Catala, O. Benomar, G. R. Davies, R. A. García, D. Salabert, J. Ballot, B. Mosser, C. Régulo, et al.

Astronomy & Astrophysics

Study of HD 169392A observed by CoRoT and HARPS[⋆,⋆⋆,⋆⋆⋆]

S. Mathur[1,2], H. Bruntt[3], C. Catala[4], O. Benomar[5], G. R. Davies[2], R. A. García[2], D. Salabert[6], J. Ballot[7,8], B. Mosser[4], C. Régulo[9,10], W. J. Chaplin[11], Y. Elsworth[11], R. Handberg[3], S. Hekker[12,11], L. Mantegazza[13], E. Michel[4], E. Poretti[13], M. Rainer[13], I. W. Roxburgh[14], R. Samadi[4], M. Stęślicki[15,1] K. Uytterhoeven[9,10], G. A. Verner[11], M. Auvergne[4], A. Baglin[4], S. Barceló Forteza[9,10], F. Baudin[16], and T. Roca Cortés[9,10]

[1] High Altitude Observatory, NCAR, PO Box 3000, Boulder, CO 80307, USA
    e-mail: savita.mathur@gmail.com
[2] Laboratoire AIM, CEA/DSM – CNRS – Univ. Paris Diderot – IRFU/SAp, Centre de Saclay, 91191 Gif-sur-Yvette Cedex, France
[3] Danish AsteroSeismology Centre, Department of Physics and Astronomy, University of Aarhus, 8000 Aarhus C, Denmark
[4] LESIA, UMR 8109, Université Pierre et Marie Curie, Université Denis Diderot, Obs. de Paris, 92195 Meudon Cedex, France
[5] Sydney Institute for Astronomy, School of Physics, University of Sydney, NSW 2006, Australia
[6] Laboratoire Lagrange, UMR 7293, Universié de Nice Sophia-Antipolis, CNRS, Observatoire de la Côte d'Azur, 06304 Nice Cedex 4, France
[7] CNRS, Institut de Recherche en Astrophysique et Planétologie, 14 avenue Édouard Belin, 31400 Toulouse, France
[8] Université de Toulouse, UPS-OMP, IRAP, 31400 Toulouse, France
[9] Instituto de Astrofísica de Canarias, 38205 La Laguna, Tenerife, Spain
[10] Universidad de La Laguna, Dpto de Astrofísica, 38206 Tenerife, Spain
[11] School of Physics and Astronomy, University of Birmingham, Edgbaston, Birmingham B15 2TT, UK
[12] Astronomical Institute Anton Pannekoek, U. of Amsterdam, PO Box 94249, 1090 GE Amsterdam, The Netherlands
[13] INAF – Osservatorio Astronomico di Brera, via E. Bianchi 46, 23807, Merate (LC), Italy
[14] Astronomy Unit, Queen Mary University of London, Mile End Road, London E1 4NS, UK
[15] Instytut Astronomiczny, Uniwersytet Wroclawski, Kopernika 11, 51-622 Wroclaw, Poland
[16] Institut d'Astrophysique Spatiale, UMR 8617, Université Paris XI, Batiment 121, 91405 Orsay Cedex, France

ABSTRACT

Context. The results obtained by asteroseismology with data from space missions such as CoRoT and *Kepler* are providing new insights into stellar evolution. After five years of observations, CoRoT is continuing to provide high-quality data and we here present an analysis of the CoRoT observations of the double star HD 169392, complemented by ground-based spectroscopic observations.
Aims. This work aims at characterising the fundamental parameters of the two stars, their chemical composition, the acoustic-mode global parameters including their individual frequencies, and their dynamics.
Methods. We analysed HARPS observations of the two stars to derive their chemical compositions. Several methods were used and compared to determine the global properties of stars' acoustic modes and their individual frequencies from the photometric data of CoRoT.
Results. The new spectroscopic observations and archival astrometric values suggest that HD 169392 is a weakly bound wide binary system. We obtained spectroscopic parameters for both components which suggest that they originate from the same interstellar cloud. However, only the signature of oscillation modes of HD 169392 A was measured; the signal-to-noise ratio of the modes in HD 169392B is too low to allow any confident detection. For HD 169392 A we were able to extract parameters of modes for $\ell = 0$, 1, 2, and 3. The analysis of splittings and inclination angle gives two possible solutions: one with with splittings and inclination angles of $0.4-1.0$ μHz and $20-40°$, the other with $0.2-0.5$ μHz and $55-86°$. Modelling this star using the Asteroseismic Modeling Portal (AMP) gives a mass of 1.15 ± 0.01 $M_\odot$, a radius of 1.88 ± 0.02 $R_\odot$, and an age of 4.33 ± 0.12 Gyr. The uncertainties come from estimated errors on the observables but do not include uncertainties on the surface layer correction or the physics of stellar models.

Key words. asteroseismology – methods: data analysis – stars: oscillations – stars: individual: HD 169392

1. Introduction

The convective motions in the outer layers of solar-like oscillating stars excite acoustic waves that become trapped in the stellar interiors (e.g., Goldreich & Keeley 1977; Samadi 2011, for a detailed review). The precise frequencies of these pressure (p)-driven waves depend on the properties of the medium in which they propagate. Thus, stellar seismology allows us to infer the properties of the Sun and stellar interiors by studying and characterising these p modes (e.g., Gough et al. 1996; Christensen-Dalsgaard 2002). However, our knowledge of the

---

properties of the stellar interiors depends on our ability to correctly measure the properties of the oscillations modes (e.g. Appourchaux et al. 1998; Appourchaux 2011).

In recent years the French-led satellite, Convection, Rotation and planetary Transits (CoRoT, Baglin et al. 2006), and NASA's *Kepler* mission (Koch et al. 2010; Borucki et al. 2010) have provided high-quality, long-term seismic data of solar-like stars. CoRoT has studied some interesting F- and G-type stars (e.g. Appourchaux et al. 2008; Barban et al. 2009; García et al. 2009; Deheuvels et al. 2010) including some that host planets (Gaulme et al. 2010; Ballot et al. 2011b; Howell et al. 2012) and others in binary systems (Mathur et al. 2010a). *Kepler* observations have enabled ensemble asteroseismology of hundreds of solar-like stars (e.g. Chaplin et al. 2011b) as well as precise studies of long time-series with more than eight months of nearly continuous data (Campante et al. 2011; Mathur et al. 2011a; Appourchaux et al. 2012b), and pulsating stars in binary systems (e.g. Hekker et al. 2010b; White et al., in prep.) and in clusters (e.g. Basu et al. 2011; Stello et al. 2011b). The fundamental properties of stars can be inferred by means of asteroseismic quantities either by using scaling relations (e.g. Kjeldsen & Bedding 1995, 2011; Samadi et al. 2007b), or by using stellar models (e.g. Piau et al. 2009; Metcalfe et al. 2010, 2012; Creevey et al. 2012; Escobar et al. 2012; Mathur et al. 2012; Mazumdar et al. 2012). This provides information on the structure of the stars and thus allows one to test stellar models and start improving the physics included in stellar evolution codes (e.g. Christensen-Dalsgaard & Thompson 2011, and references there in).

In the present paper we report the study of the double star HD 169392, using high-resolution spectrophotometry by HARPS combined with seismic analysis from CoRoT photometry. However, in this latter case, only HD 169392A was analysed because HD 169392B was too faint. The two components of HD 169392≡WDS 18247-0636 have a separation of $5.881 \pm 0.006''$, a position angle of $195.08 \pm 0.09°$, and a magnitude difference $\Delta V = 1.507 \pm 0.002$ at the epoch 2005.48 (Sinachopoulos et al. 2007). The two components are reported in SIMBAD[1] as having similar proper motions. HD 169392A≡HIP 90239 is the main component of the pair, with spectral type G0 IV and a parallax $\pi = 13.82 \pm 1.20$ mas (van Leeuwen 2007). From the Geneva-Copenhagen survey (Nordström et al. 2004; Holmberg et al. 2007) this primary star has $T_{eff} = 5942$ K, [Fe/H] = -0.03, $m_V = 7.50$ mag, and $v \sin i = 3$ km s^{-1}. The second component of the system, HD 169392B (Duncan 1984), is a G0 V – G2 IV star with $m_V = 8.98$ mag.

New spectroscopic observations performed by HARPS (Mayor et al. 2003) that are detailed in Sect. 2 have allowed a precise characterisation of the stellar properties of the two stars in the system. In Sect. 3, we describe the methodology used to prepare the original time series from CoRoT data, to fit the mode oscillation power spectrum, and to derive a single frequency set from results of different fitters. In Sect. 4 we investigate the global properties of the modes of both stars while in Sect. 5 we analyse the surface rotation and the background of HD 169392A. In Sect. 6, we present the peak-bagging methods used to obtain the frequencies of the individual p modes of HD 169392A and the results are discussed in Sect. 7. With the derived spectroscopic constraints and mode frequencies we model the star and derive the fundamental parameters of HD 169392A in Sect. 8. The main results are summarised in Sect. 9.

---

[1] This research has made use of the SIMBAD database, operated at CDS, Strasbourg, France.

2. Fundamental stellar parameters

High-quality spectra of HD 169392 were collected as part of the activities of the CoRoT ground-based observations working group (e.g. Catala et al. 2006; Uytterhoeven et al. 2008; Poretti et al. 2012). We obtained high signal-to-noise ratio (S/N) spectra of each component using HARPS in high-resolution mode ($R = 114\,000$). The spectrum of HD 169392A taken on the night of 25−26 June 2011 shows a radial velocity (RV) of -68.1606 ± 0.0004 km s^{-1}, while that of HD 169392B (taken on the night of 24−25 June 2011) shows an RV = -70.1388 ± 0.0004 km s^{-1}. To have the common proper motions and compatible radial velocities are sufficient to consider a double star as a physical pair (e.g. Struve et al. 1955). In the case of HD 169392, the separation of $0.0588''$ at a distance of 723 pc corresponds to 4250 AU, implying that the system should be weakly gravitationally bound.

The HARPS spectra both have excellent S/N, i.e., $S/N = 267$ for the A component, and 234 for the B component. They were reduced using a MIDAS semi-automatic pipeline Rainer (2003). Their high quality allowed a careful and detailed analysis with the semi-automated pipeline VWA (Bruntt et al. 2010). More than 400 spectral lines were analysed in each star. The match of each synthetic line profile to the observations was cross-checked by eye and several lines were rejected either due to problems with the placement of the continuum or due to strong blends in the line wings. Atmospheric models were determined by interpolating on a grid of MARCS models (Gustafsson et al. 2008) and line data were extracted from VALD (Kupka et al. 1999). The oscillator strengths ($\log gf$) were adjusted relative to a solar spectrum, as described by Bruntt et al. (2012).

The classical analysis method involves treating the effective temperature, T_{eff}, the surface gravity, $\log g$, and microturbulence, v_{macro} as free parameters. The optimum solution is then selected by minimizing the correlation between the Fe I abundance, equivalent width, and excitation potential. Furthermore, we required that the mean abundances determined from neutral and ionised Fe lines agreed. The final parameters are listed in Table 1. For these parameters we calculated the abundances of 13 different species. We performed the analysis with and without the seismic $\log g$, which is available only for the A component (see Sect. 4.1). When the seismic value was used, it affected the $\log g$ value by +0.2 dex and T_{eff} by +100 K. We also note that [Fe/H] was increased by about 0.05 dex.

Table 2 lists the abundances relative to the Sun (ΔA), along with the number of spectral lines used in the analysis. The abundances are also plotted in Fig. 1. The lithium abundance was determined for both components of the system: [Li/H]$_A$ = $+1.42 \pm 0.10$ and [Li/H]$_B$ = $+0.23 \pm 0.12$ (see details in Bruntt et al. 2012). According to the temperatures of both stars, the measured lithium abundances are consistent with the sample analysed by Israelian et al. (2004).

We adjusted the projected splittings, $v \sin i$, by fitting the observations to synthetic line profiles, using several isolated lines. The macroturbulence parameter was fixed using the calibration for solar-type stars from Bruntt et al. (2010). We note that the metallicities of the two components are quite similar.

2.1. Deriving ν_{max} from spectroscopic parameters

The proportionality between the frequency at maximum power, ν_{max}, and the acoustic cutoff frequency was originally suggested by Brown et al. (1991), developed by Kjeldsen & Bedding (1995), and justified theoretically by Belkacem et al. (2011). The large frequency spacing, $\Delta \nu$, is to good

Table 1. Spectroscopic parameters for the A and B components of the system, as derived from HARPS data and the seismic $\log g$.

	A	B	Units
T_{eff}	5985 ± 60	5885 ± 70	K
$\log g$	3.96 ± 0.07	3.75 ± 0.07	cgs
[Fe/H]	-0.04 ± 0.10	-0.10 ± 0.10	dex
v_{micro}	1.41 ± 0.07	1.04 ± 0.07	km s^{-1}
$v \sin i$	1.0 ± 0.6	3.0 ± 0.7	km s^{-1}
v_{macro}	2.8 ± 0.4	2.5 ± 0.4	km s^{-1} (fixed)

Table 2. Abundances relative to the Sun (ΔA) and the number of lines (N) used in the spectral analysis of the two components (A and B) of the system.

Element	ΔA(A) (dex)	N (A)	ΔA(B) (dex)	N (B)
Li I	$+1.42$	1	$+0.23$	1
C I	-0.09	4	-0.00	3
Si I	-0.05	25	$+0.02$	29
Si II	-0.06	1		
S I	-0.04	3	-0.00	3
Ca I	-0.04	13	$+0.05$	10
Sc II	-0.02	5	$+0.06$	4
Ti I	-0.07	28	$+0.01$	43
Ti II	-0.01	12	$+0.02$	8
V I	-0.06	8	$+0.01$	11
Cr I	-0.07	22	-0.01	23
Cr II	-0.11	4	-0.00	6
Fe I	-0.06	239	$+0.03$	233
Fe II	-0.03	22	$+0.03$	20
Co I	-0.15	6	-0.00	7
Ni I	-0.08	64	$+0.02$	75
Y II	-0.08	4	-0.06	3
Ce II	-0.08	2	$+0.00$	2

Notes. The abundances have an uncertainty of 0.08 dex for all elements except for lithium, whose abundances are 0.10 and 0.12 for the A and the B components, respectively.

approximation proportional to the square root of the mean density of the star. The scaling relations – scaled to solar values – have also been extensively tested with observational data (e.g. Huber et al. 2011). The relations allow us to obtain approximate values for the so-called mean "large spacing", $\langle \Delta\nu \rangle$, and the frequency of maximum amplitude ν_{max}.

Combining both equations, we are able to predict ν_{max} for both components, using the effective temperature and the $\log g$ in Table 1. Taking into account the uncertainties in the spectroscopic parameters, the predicted ν_{max} lie in the range [524, 730] μHz (HD 169392A) and [2202, 3077] μHz (HD 169392B).

3. CoRoT photometric light curve

CoRoT observed HD 169392 (CoRoT ID 9161) continuously during a period of 91.2 days spanning the epoch 2009 April 1 through 2009 July 2. These observations were made as part of the third long run in the central direction of the galaxy (LRc03). In the present study, we used the so-called *helreg* level 2 (N2) datasets (Samadi et al. 2007a), i.e., time series prepared by the CoRoT Data Center (CDC) that have a regular cadence of 32 s in the heliocentric frame.

During the crossing of the South Atlantic Anomaly (SAA), the CoRoT measurements are perturbed (Auvergne et al. 2009) and the frequency-power spectrum shows a sequence of spikes
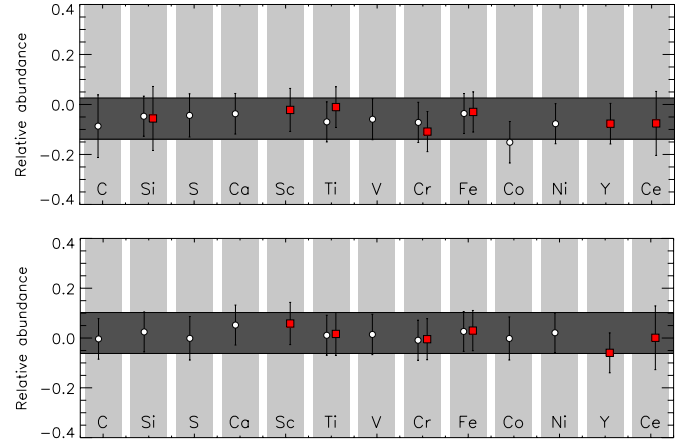
Fig. 1. Abundances, relative to the Sun, for 14 elements in the A (*top*) and B (*bottom*) components of the system. Circles and box symbols are used for the mean abundance from neutral and singly ionised lines, respectively. The dark grey horizontal bar marks the mean metallicity within a 1-σ uncertainty range. Lithium is not plotted because it has a much higher value than the other elements in the A component.
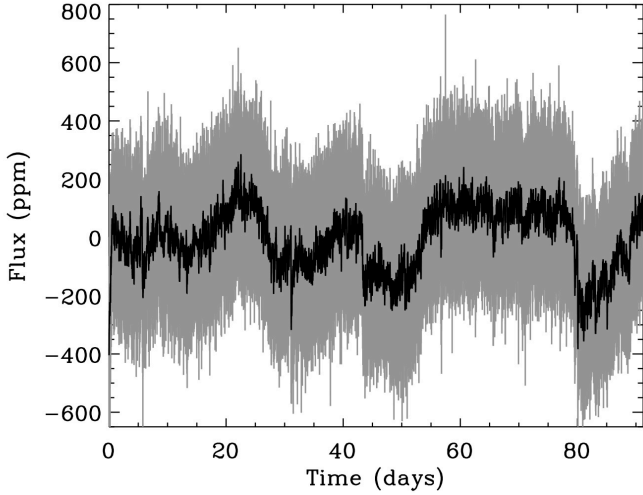
at frequencies of $n \times 161.7 \, \mu$Hz, where n is an integer. Moreover, other spurious peaks appear at multiples of daily harmonics at $(n \times 161.7) \pm (m \times 11.57) \, \mu$Hz, where m is an integer. Various teams in the collaboration used different interpolation techniques to replace the perturbed data. One method employed an "inpainting" algorithm – a multi-scale discrete cosine transform (Sato et al. 2010) – that yielded robust results on other CoRoT targets (see for example HD 170987, Mathur et al. 2010a). The overall duty cycle before interpolation was 83.4%. Another method was to interpolate the gaps produced by SAA with parabola, extended from fits made to points around the gap, in a way similar to the usual interpolation performed in N2 data for missing points (see Ballot et al. 2011b, for details).

The measured light curve was converted into units of relative flux (ppm) by correcting first for any discontinuity in the flux and then removing a sixth-order polynomial fit to take into account the aging of the instrument (Auvergne et al. 2009). The resulting flux is plotted in Fig. 2. Two jumps – possibly of instrumental origin – are visible at the times 43.3 and 80.05 days from the beginning of the lightcurve. Although they have no significant influence on the power spectral density (PSD) (power is introduced over a range of frequencies, owing to the sharp nature of the features in time), they have a considerable impact on the analysis of the surface rotation (see Sect. 5.2). To compute the PSD, we used a standard fast Fourier transform algorithm, and normalised it so as to satisfy Parseval's theorem for one-sided power spectral density (Press et al. 1992).
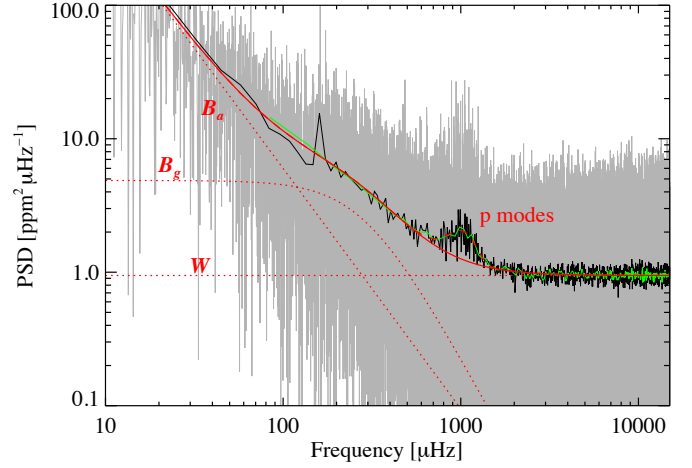
4. Global seismic parameters of the binary system

4.1. HD 169392A

Three different teams, A2Z, COR, and OCT, analysed the global seismic properties of HD 169392A using different methodologies. Explanations of each method may be found in Mathur et al. (2010b), Mosser & Appourchaux (2009), and Hekker et al. (2010a). Each team estimated the mean large frequency spacing, $\langle \Delta\nu \rangle$, the frequency of maximum power in the p-mode bump, ν_{max}, and the maximum amplitude per radial mode, converted to bolometric amplitude following the method described in Michel et al. (2009), $A_{\mathrm{bol},l=0}$.

Fig. 2. N2-helreg relative flux (in grey) after inpainting the bad points (see text), including those taken during the SAA crossing. The aging was removed by a sixth-order polynomial fit. The black curve corresponds to a one-hour rebin.

Table 3. Global seismic parameters computed using the A2Z pipeline.

Quantity	Value	Units
$\langle \Delta \nu \rangle$	56.32 ± 1.17	μHz
ν_{max}	1030 ± 54	μHz
$A_{bol,l=0}$	3.61 ± 0.35	ppm

The results from A2Z are summarized in Table 3. Briefly, the A2Z and OCT methods analyse the power spectrum of the power spectrum to measure the mean large separation, while the COR method computes the envelope autocorrelation function of the time series. All teams show good agreement on the values of the seismic parameters when we take into account the different frequency ranges that were used for the analyses (a full comparison of the pipelines, as applied to a large sample of *Kepler* targets, may be found in Hekker et al. 2011; and Verner et al. 2011).

In the A2Z pipeline, the values of ν_{max} and $A_{bol,l=0}$ were obtained by smoothing the background-subtracted PSD with a sliding window of width $2\langle \Delta \nu \rangle$ as described by Kjeldsen et al. (2008a). Then, to derive $A_{bol,l=0}$ we followed the procedure to correct for the CoRoT instrumental response as described in Michel et al. (2008), while ν_{max} corresponds to the frequency of the maximum power of a fitted Gaussian.

By scaling against solar parameters, (e.g. Kjeldsen & Bedding 1995) and using the effective temperature derived by our HARPS observations (see Table 1), we may infer some seismic stellar parameters. We obtain a mass of 1.34 ± 0.26 $M_\odot$, a radius of 1.97 ± 0.19 $R_\odot$, and a log g of 3.96 ± 0.013 dex.

4.2. Looking for HD 169392B

We noted in Sect. 2.1 that the maximum of the p-mode bump for HD 169392B should lie around a region centred at $\sim$2650 μHz. Five different teams looked for the signature of this second star without advance knowledge of this prediction, but failed to detect any modes.

Using the stellar parameters of the two components (T_{eff}, m_V, R), we computed the probability of detection of the

Fig. 3. PSD of HD 169392 data (grey) that was modelled as explained in the text (red curves) with the usual three components: white noise (W), granulation noise (B_g), and stellar activity and/or large scales of convection (B_a). The red continuous line is the sum of these three components, resulting from the fit of the smoothed spectrum over $\Delta \nu$ (green line). The black curve corresponds to the spectrum smoothed over 101 bins, i.e. 12.8 μHz.

modes following the method described in Chaplin et al. (2011a). For the A component, we obtain a 100% probability of detection, consistent with the data, which show a clear spectrum of oscillations. For the B component, whose flux is dimmed by the A component by 80%, and by assuming a radius of $\sim$1.03 $R_\odot$ and a mass of $\sim$1 $M_\odot$ from the scaling relations, we obtain a probability of only 2% to detect the modes, consistent with non-detection from the CoRoT data.

We focus in the remainder of the paper on the A component of the system.

5. Background and surface rotation of HD 169392A

5.1. Stellar background

The flux from the star is measured at a regular cadence. We computed the PSD from the light curve using a fast Fourier transform algorithm. The resulting spectrum is plotted in Fig. 3 (grey line). The PSD rebinned over 12.8 μHz (101 bins) and over the large separation are also shown (black and green lines in Fig. 3).

A single p-mode bump that corresponds to HD 169392A is clearly visible. The convective background (red curve in Fig. 3) was fitted using a standard maximum-likelihood estimator (MLE) with three standard components: a white noise (W), one Harvey law (Harvey 1985), and one power law (see for more details, e.g., Mathur et al. 2011b),

$$B(\nu) = W + \frac{4\tau_g \sigma_g^2}{1 + (2\pi\tau_g\nu)^{\alpha_g}} + P_a\nu^{-e_a},$$ (1)

where τ_g and σ_g are the characteristic time scale and amplitude of the granulation, and α_g and e_a are the exponents characterizing the temporal coherence of the phenomenon. We obtained the following coefficients: $W = 0.945 \pm 0.003$ ppm^2/μHz, $\tau_g = 557 \pm 60$ s, $\sigma_g = 46.8 \pm 2.1$ ppm, $\alpha_g = 2.43 \pm 0.18$, $P_a = 24 \pm 4.3$, and $e_a = 1.8 \pm 0.06$. The value obtained for the granulation time scale is consistent with the relationship with ν_{max} (Mathur et al. 2011b) previously derived for the *Kepler*

red giants. Finally, we also computed the rms amplitude of the granulation:

$$\sigma_{g,rms} = \sigma_g / \sqrt{\frac{\alpha_g}{2} \sin\left(\frac{\pi}{\alpha_g}\right)} \qquad (2)$$

and obtain $\sigma_{g,rms} \approx 43.3 \pm 2.2$ ppm. Nevertheless, we have to keep in mind that this measurement is polluted by the secondary star of the binary system. There are two opposite effects that tend to reduce the impact of the secondary. On the one hand, HD 169392B contributes 20% to the total observed flux (see also Sect. 7.6). This translates into an underestimation of $\sigma_{g,rms}$ by a similar amount. On the other hand, the granulation component measured for HD 169392A probably includes a contribution from the granulation (and other short-frequency variabilities) of HD 169392B. This would lead to an overestimation of $\sigma_{g,rms}$.

5.2. Surface rotation

Magnetic features such as starspots crossing the visible stellar disk of a star produce a fluctuation of the flux emitted by the star. The careful analysis of these long-period modulations in the observed light curve provides invaluable information on the average rotation rate of the surface of the star at the latitudes where these magnetic features evolve. This study can be performed directly in the light curve by modelling the spots (e.g. Mosser et al. 2009b,a), or by close inspection of the low-frequency part of the power spectrum (e.g. García et al. 2009; Campante et al. 2011).

Looking at the light curve displayed in Fig. 2, we do not see any clear modulation produced by spots. However, the low-frequency part of the power spectrum is dominated by two significant peaks at 0.25 and 0.64 μHz (see black line of Fig. 4), the latter being a harmonics of the first peak when we consider the frequency resolution of 0.127 μHz. But as explained in Sect. 3, there are two jumps of possible instrumental origin at 43.3 and 80.05 days that could be at the origin of the peak at 0.25 μHz. To verify this hypothesis, we corrected the jumps with the same procedure that was used to correct *Kepler* data (García et al. 2011). In the PSD of the resulting light curve (blue line in Fig. 4) there is no power at the above mentioned frequencies. Therefore, it is probable that the 0.25 and 0.64 μHz peaks have been produced by instabilities in CoRoT but a stellar origin could still be possible.

6. Methodology followed to extract the mode parameters of HD 169392A

Nine teams estimated the mode parameters for HD 169392A with two teams providing two sets of results from differing methods. This gives a total of eleven sets of mode parameters. We describe, albeit briefly, the methods used by the different teams to fit the power spectrum corrected from the background. A list of the methods used for each of the sets of mode parameters can be found in Table 4.

All teams used a common philosophy for estimating mode parameters: maximise the likelihood function for a given model. The models used by the teams are common in that all are composed from a sum of Lorentzian profiles to describe the modes of oscillation, plus a background to account for the instrumental and stellar noise (see Sect. 5.1). Each team used the frequency, height, linewidth, rotational splitting, and angle of inclination to describe a mode of oscillation (e.g. Appourchaux et al. 2008). All teams fitted a single linewidth for each order. The main differences between teams arise from the method used to maximise
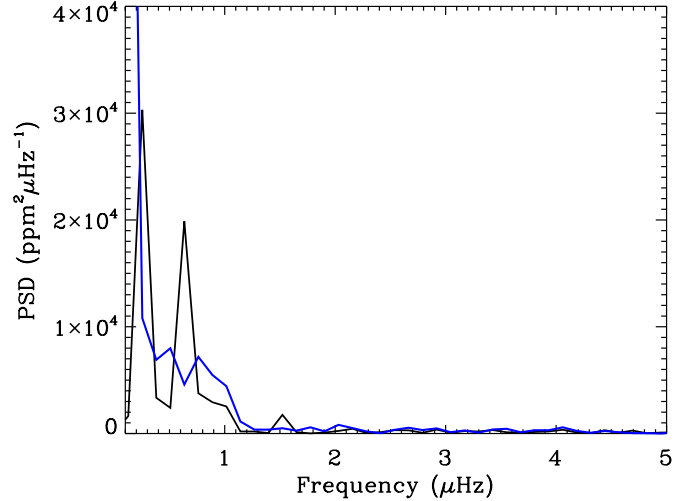
Fig. 4. Low-frequency part of the power spectrum between 0.1 and 5 μHz. The black line corresponds to the light curve shown in Fig. 2. Two peaks are visible at 0.25 and 0.64 μHz. The blue line corresponds to the PSD of the light curve in which the jumps at 43.3 and 80.05 days were corrected.

Table 4. Description of the fitting methods of each team.

Fitter ID	Method	Splittings	Angle
OB[a]	MCMC global	Free	Free
JB[b]	MAP global	Free	Free
GRD[b]	MAP global	Free	Free
RAG[b]	MLE global	Free	Free
RAG[b]	MLE global	Fixed 0	Fixed 0
SH[c]	MLE pseudo-global	Free	Free
RH[d]	MCMC global	Free	Free
CR[b]	MLE global	Free	Free
CR[b]	MLE global	Fixed 0	Fixed 0
DS[e]	MLE local	Free	Free
GAV[b]	MLE global	Free	Free

Notes. [a] Benomar (2008); [b] Appourchaux et al. (1998); [c] Fletcher et al. (2011); [d] Handberg & Campante (2011); [e] Salabert et al. (2004).

the likelihood. The three main categories used are maximum-likelihood estimation (MLE, Appourchaux et al. 1998), which has a variant called the maximum a posteriori method (MAP, Gaulme et al. 2009), and the Markov chain Monte Carlo method (MCMC, Benomar 2008; Handberg & Campante 2011).

The MLE or the MAP approaches were used by the majority of teams. Briefly, MLE estimates the mode parameters by performing a multi-dimensional maximisation of the likelihood parameter. Typically, formal one-sigma errors are determined from the Hessian matrix. Like all Bayesian approaches, MAP techniques extend this concept by including a priori knowledge by implementing penalties on the likelihood parameter for defined regions of parameter space. As for MLE, MAP errors are taken from the Hessian matrix. Both MLE and MAP can be applied either globally, that is, simultaneously fit to the entire frequency range (e.g. Appourchaux 2008), or locally, considering parameters separately over one large separation (Salabert et al. 2004). When coupled with MCMC, a Bayesian approach is a powerful way (but also time-consuming) to extract the full statistical information with respect to the likelihood and our prior knowledge by mapping the probability density function (PDF) of each parameter. In contrast to MLE or MAP, MCMC techniques

avoid becoming trapped in local maxima and no assumptions on the nature of the probability density function are needed. Consequently, this approach provides more conservative and robust results, especially for the uncertainties, as their estimation does not rely on the Hessian matrix, but on the cumulative distribution function, built thanks to the PDF. In the present paper, two fitters (OB, RH) used MCMC approaches with different priors. However, a careful choice of the priors was needed because they might have a strong impact on the best-fitted parameters, especially at low S/N. This star is a perfect example: $\ell = 0$ and $\ell = 2$ frequencies lower than 870 μHz (the three first radial orders) could barely be fitted (posterior probability highly multimodal and non-Gaussian) if no smoothness condition was applied onto the frequencies of these modes. A smoothness condition acts as a filter and avoids strong, erratic variations of frequencies from one order to another (Benomar et al. 2012).

Each of the three approaches can be applied in slightly different ways. Two fitters (RAG and CRR) produced two (MLE/MAP) results with and without the two parameters describing rotation rate and angle of inclination. No mode profile asymmetry was included for any case in this analysis. This is due to the insufficient S/N: asymmetry fitting requires a very good S/N and high resolution.

The analysis revealed the presence of mixed modes. As a consequence, to complement the fitting techniques, we also used the asymptotic relation found by Goupil (priv. comm.), following the ideas originally developed by Unno et al. (1989) and tested by Mosser et al. (2012). This methodology is particularly suited to identify the presence of mixed modes in the power spectrum and to derive the measure of the gravity period spacing. This global seismic parameter provides a strong constraint on the core radiative region of the interior models.

Given eleven sets of fitter results, we required a statistically robust method of comparison to produce a final list of mode parameters for future modelling. Here we adapted a previously used method (Appourchaux et al. 2012b) to determine a confident list of mode frequencies. This method used an iterative outlier rejection algorithm to populate two lists (a maximal and a minimal list) of modes, which were then used to determine the "best" fitter who will provide the frequencies and is defined as the fitter with the smallest normalised rms deviation from the average frequency.

At each radial order, n, and degree, l, we compared N different estimated frequencies. As a first cut a visual inspection of all mode parameters and errors was performed. Modes with clearly incorrect parameters (for example, very small/large linewidths or very large errors) were rejected. Statistical outlier rejection was performed with Peirce's criterion (Peirce 1852; Gould 1855), a method that is based on rigorous arguments. Peirce's criterion was applied iteratively to each mode frequency set until no data points are rejected. The method can be described with the following pseudo-code:

- COMPUTE mean $\bar{x}$ and rms σ deviation from the sample x.
- COMPUTE rejection factor r from Gould (1855) assuming one doubtful observation.
- REJECT: Reject data if $|x_i - \bar{x}| > r\sigma$.
- IF n data are rejected THEN compute new r assuming $n + 1$ doubtful observations ELSE END.
- GOTO REJECT.

With the results of the outlier rejection we populated the maximal and minimal list in the following way. The minimal list was designed such that we had a very high level of confidence in the results included. Previous works have used varying threshold criteria for inclusion in the minimal list. Metcalfe et al. (2010) required that all fitters agree to place a frequency in the minimal list, i.e. N results are accepted. In an updated version of the recipe, (Campante et al. 2011) and Mathur et al. (2011a) required that $N/2$ results are accepted. Here we followed the $N/2$ acceptance criterion for the minimal list. Modes forming the maximal list must have at least two results accepted by Peirce's criterion; because of this, the maximal list must be treated with some caution.

In the maximal and minimal lists we selected the actual frequencies of the modes in each list. We calculated the normalised root-mean-square (RMS) deviation of the N teams with respect to the mean of the frequencies for each mode in the minimal list (see Eq. (2) of Mathur et al. 2011a). The data set with the lowest normalised RMS deviation was declared the "best" fitter. Two methods (MLE and MCMC) obtained very similar values of RMS and we decided to present in the following sections the results obtained by the MCMC, providing a reproducible set of frequency parameters.

7. Results

Following the methodology described in the previous section, we obtained the mode parameters presented in this section.

7.1. Mode frequencies

A comparison of the 11 sets of mode frequencies provided by the nine teams gave the minimal and maximal lists of frequencies. The fitter selected from the smallest RMS deviation (namely OB) used the MCMC algorithm and the model fitting the data is represented in Fig. 5. We obtained a minimal list of 25 modes. The maximal list contains four additional modes. The lower panel of Fig. 5 shows the ratio of the power spectrum to the fitted model. The power spectrum can be thought of as composed of a limit spectrum multiplied by a χ^2 with a two degree-of-freedom noise function (e.g. Anderson et al. 1990). When it is smoothed over k bins, the noise function is distributed as a χ^2 with $2k$ degrees of freedom (e.g. Appourchaux et al. 1998). If the fitted model describes the limit spectrum well, the ratio of the power spectrum to the model will be distributed as the noise function. Hence, the power spectrum normalised by the model in the lower panel of Fig. 5 reveals structures in the power spectrum that are not compensated for by the fitted model in the region where the $\ell = 3$ modes are expected (shown with arrows in the plot).

7.2. $\ell = 3$ modes

With the MCMC technique, we fitted the $\ell = 0$, 1, 2, and 3 simultaneously. We checked that the frequencies of the modes $\ell = 0$, 1, and 2 remain unchanged. In Table 5, we give the minimal and maximal lists of frequencies as well as the three $\ell = 3$ modes that have a significant posterior probability. However, we recall that these modes have to be taken very cautiously. By extending the fit to the $\ell = 3$ modes, it slightly modified the final values of the amplitudes, widths, splittings, and inclination angle. The values listed in Table 7 correspond to the fitting of the four ridges.

7.3. Mixed modes

By looking at the échelle diagram (Fig. 6), we notice an avoided crossing, corresponding to the presence of a mixed mode (e.g.
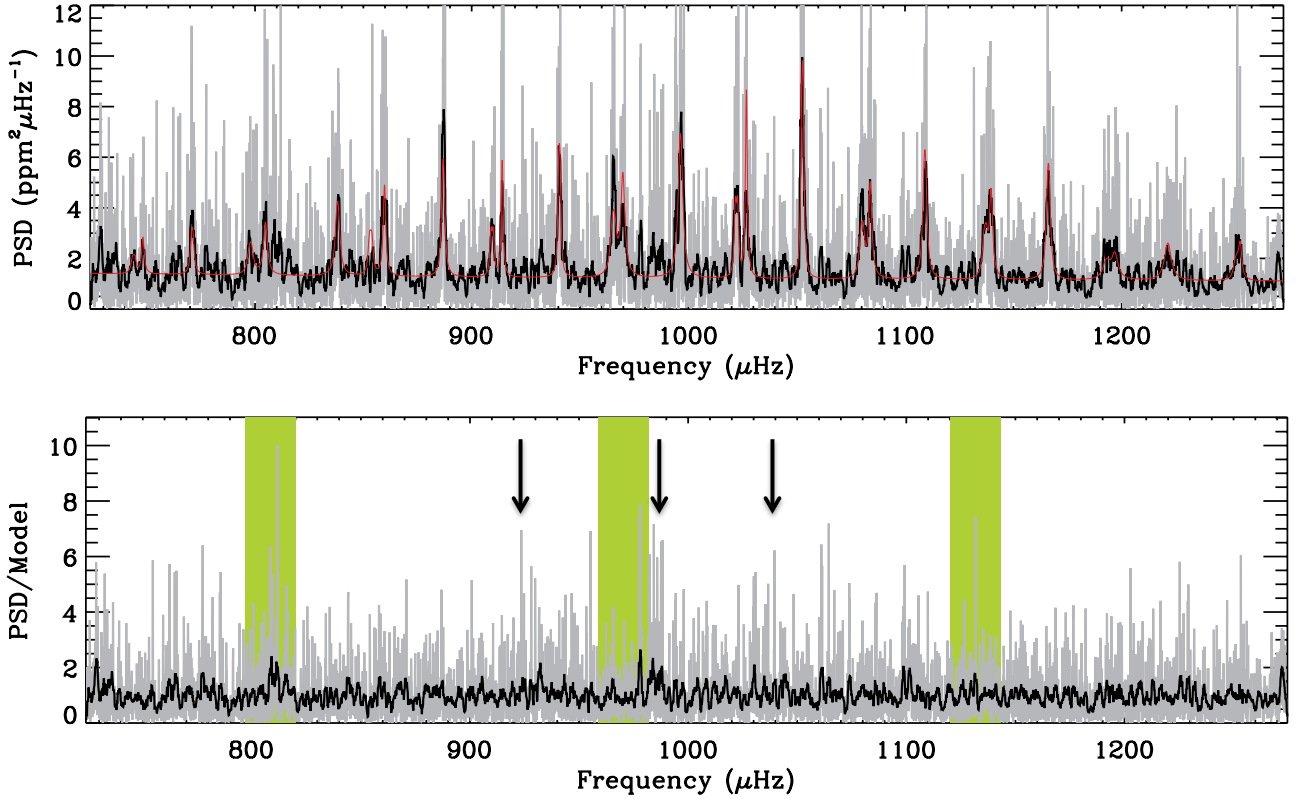
Fig. 5. *Upper panel*: PSD of HD 169392 in the p-mode region at full resolution (grey) and smoothed over 15-bin wide boxcar (black). The red line corresponds to the fitted spectrum from refit after the frequency comparison stage. *Lower panel*: power spectral density for the p-mode region divided by the fitted model at full resolution (grey) and smoothed over 15 bins (black). Regions highlighted in green cover the regions corresponding to the harmonics of the CoRoT orbital period such that $\nu = (n \times 161.7) \pm (m \times 11.5)\,\mu$Hz, where n and m are integers. The arrows show the positions where we would expect $\ell = 3$ modes.
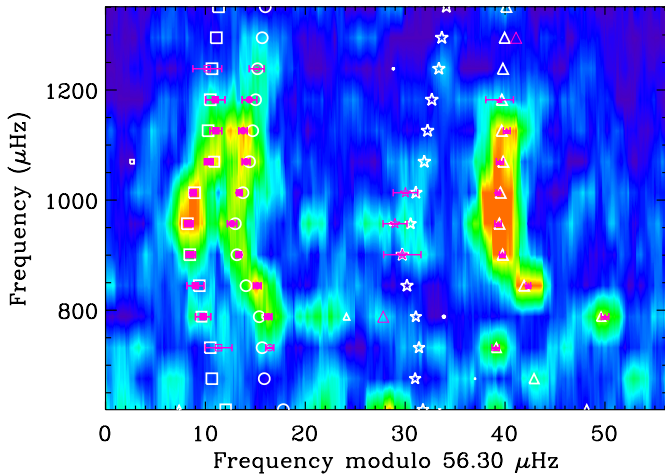
Fig. 6. Échelle diagram of the CoRoT target, HD 169392A, with the minimal (close pink symbols) and maximal (open and close pink symbols) lists of frequencies, and the frequencies from the best-fit model of AMP (white symbols): $\ell = 0$ (circles), $\ell = 1$ (triangles), $\ell = 2$ (squares), and $\ell = 3$ (stars) as in Sect. 7.2. The pink triangles without uncertainties correspond to the mixed modes ($\ell = 1$) mentioned in Sect. 7.3.

Osaki 1975; Aizenman et al. 1977; Deheuvels & Michel 2011). The frequency pattern is affected by the coupling of the pressure wave in the outer convective region with a gravity wave in the radiative interior. Hence, we can use the formalism developed for mixed modes in giants (Mosser et al. 2012) to describe this pattern.

Table 6. Mixed-mode parameters.

Asymptotic p modes		
Pressure phase offset	ε_{p}	1.17 ± 0.02
Small separation	d_{01}	0.03 ± 0.02
Curvature	α	0.0029 ± 0.0008
Asymptotic g modes		
Gravity period spacing	$\Delta\Pi_1$	476.9 ± 4.3 s
Gravity phase offset	ε_{g}	0.07 ± 0.03
Mixed modes		
Coupling	q	0.098 ± 0.005

For p modes, the second-order correction of the asymptotic relation is related by a curvature term α:

$$\nu_{n_{\mathrm{p}},\ell} = \left(n_{\mathrm{p}} + \frac{\ell}{2} + \varepsilon_{\mathrm{p}} - d_{0\ell} + \frac{\alpha}{2}[n_{\mathrm{p}} - n_{\max}]^2\right)\Delta\nu, \quad (3)$$

where ε_{p} is the pressure phase offset, $d_{0\ell}$ accounts for the small separation, and $n_{\max} = \nu_{\max}/\Delta\nu$. The g modes are reduced to the first-order term:

$$P_{n_{\mathrm{g}},\ell=1} = (|n_{\mathrm{g}}| + \varepsilon_{\mathrm{g}})\,\Delta\Pi_1, \quad (4)$$

where n_{g} is the gravity radial order, ε_{g} the gravity phase offset, and $\Delta\Pi_1$ the gravity period spacing of dipole modes.

The coupling of the p and g waves is then expressed by a single constant (Mosser et al. 2012). Table 6 shows the asymptotic parameters used for the fit. Compared to modes in giants that have very large gravity orders (in absolute value), mixed modes
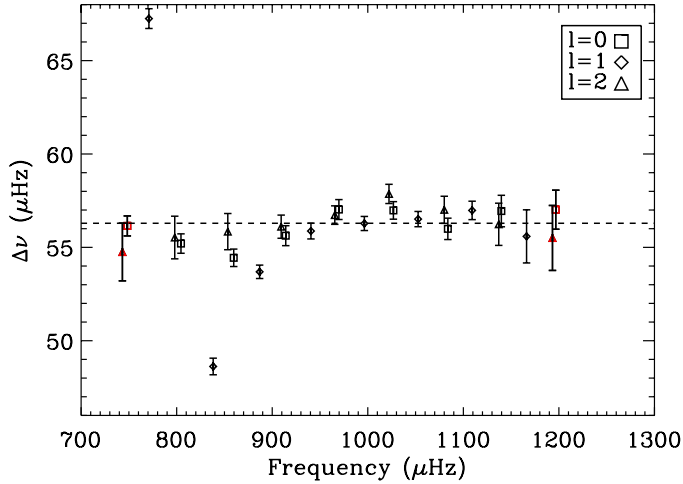
Fig. 7. Large separation as a function of frequency for $\ell = 0$, 1 and 2. The dashed line represents the mean large separation of the radial modes. The red squares at low- and high frequency represent the values obtained using the modes of the maximal list.

Fig. 8. Small separation, δ_{02}, as a function of frequency. The red squares at low- and high frequency represent the values obtained using the modes of the maximal list.

in a subgiant with $\Delta\nu \simeq 56~\mu$Hz have small $|n_g|$. Therefore, we cannot consider the asymptotic constant ε_g to be 0.

The best fit of the radial ridge, obtained from a global agreement over nine orders, is provided with $\Delta\nu = 56.3~\mu$Hz and $\varepsilon_p = 1.17$. We then infer a gravity period spacing of approximately 476.9 ± 4.3 s, with a precision limited by the uncertainty on the unknown gravity offset. Best fits are obtained with $\varepsilon_g = 0.07 \pm 0.03$. In all cases, the coupling is small: $q = 0.098 \pm 0.005$. Two mixed modes are reported at 816 and 1336 μHz with gravity orders of -2 and -1, respectively, corresponding to the period of g modes (the avoided crossing), $P_g = (|n_g| + 1/2 + \varepsilon_g)\,\Delta\Pi_1$ (Goupil et al., in prep.). These mixed modes bring strong constraints on the age of a star as the coupling between the p- and g-mode cavities changes quickly with stellar age, yielding strong constraints on the age of the star (e.g. Christensen-Dalsgaard 2004; Metcalfe et al. 2010; Mathur et al. 2012). The presence of the mixed modes in HD 169392A indicates that this star is quite evolved.

Unfortunately, none of these two modes were fitted by the nine teams. The peak at 816 μHz is surrounded by the orbital harmonics and without a proper modelling of these peaks, it is not possible to fit the mixed mode. The high-frequency mixed mode at 1336 μHz has too weak a signal to be fitted.

7.4. Frequency differences

We fitted the frequencies of the $\ell = 0$ modes against the order n and according to Eq. (3), the slope is the mean large frequency separation. We obtained $\langle\Delta\nu\rangle = 55.98 \pm 0.05~\mu$Hz, which agrees with the value obtained from the global techniques (see Sect. 4) and the mixed-mode asymptotic fit (Sect. 7.3). The variation of the mean large separation is shown in Fig. 7. We notice the dip for the modes $\ell = 1$, due to the avoided crossing mentioned above. The low oscillation we observe is typical of the signature we can have for the second helium ionisation zone below the stellar surface. We would need more modes to be able to extract the position this ionisation zone.

We also computed the variation of the small separation between $\ell = 0$ and 2 following Roxburgh & Vorontsov (2003), which is shown in Fig. 8. The small separation presents a general decreasing trend (with a slope of -0.007), which is very
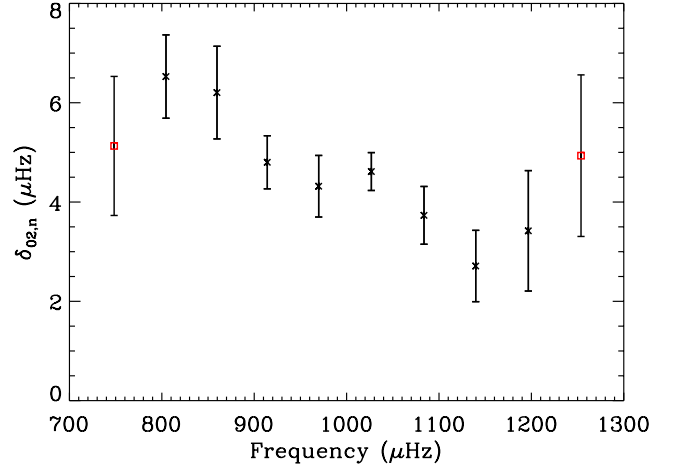
similar to what we observe on the Sun. The mean value is around 4.14 μHz. This value perfeclty fits the CD diagram presented by White et al. (2011) where for subgiants the small separation is approximately the same as for stars with very different masses.
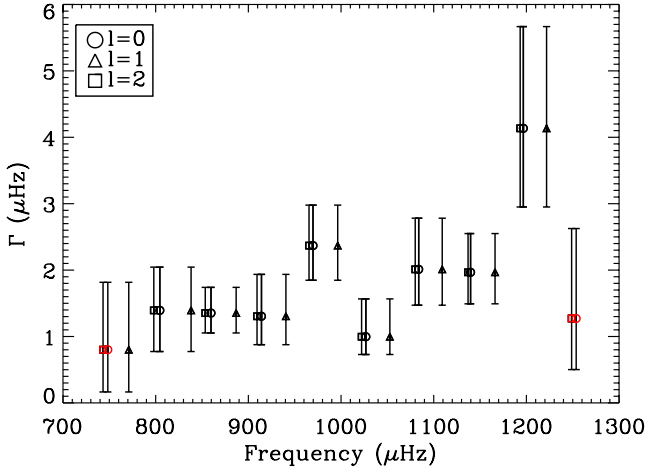
7.5. Linewidths

The linewidths of the modes ($\Gamma_{\ell,n}$) as measured in the power spectrum are related to their lifetimes ($\tau_{\ell,n}$) as indicated next for a mode of degree $\ell = 0$ and order n:

$$\tau_{0,n} = (\pi\Gamma_{0,n})^{-1}, \tag{5}$$

The results from the MCMC method, which fitted a single linewidth for $\ell = 0$, 1, and 2 modes per order, are given in Table 7 and are represented in Fig. 9. We note that the trend is rather flat with a median value of 1.8 μHz, with a little increase with frequency. The first and last points were obtained with the frequency of the maximal list of modes. This behaviour is similar to the one found in the Sun in the plateau region and the higher frequencies. We also observe a low oscillation followed by a small increase of the linewidth, which is also seen in other G-type stars observed by CoRoT (e.g. Deheuvels et al. 2010; Ballot et al. 2011b).

There have been several projects that aimed to show a power-law dependence of the linewidths on the effective temperature of the star as $\Gamma \sim T_{\rm eff}^s$. Chaplin et al. (2009) derived a relationship indicating that the mean linewidth should scale as $T_{\rm eff}^4$ for temperatures ranging between 6800 K and 5300 K. Later work by Baudin et al. (2011) using five main-sequence stars observed by CoRoT plus the Sun re-evaluated the exponent to be 16 ± 2. Recently, Appourchaux et al. (2012a) used an analysis of 42 cool main-sequence stars and subgiants observed by *Kepler* to refine the expression to $\Gamma \sim T_{\rm eff}^{15.5}$. For HD 169392, we measure the linewidth at maximum height as 1.41 μHz ($\ell = 0$, $n = 18$), a value that agrees very well with Fig. 2 of Appourchaux et al. (2012a) using $T_{\rm eff} = 5885$ K and with the theoretical computation by Belkacem et al. (2012). Finally, Corsaro et al. (2012) analysed the linewidth of red-giant stars in clusters and found that by taking into account main-sequence and subgiant stars, Γ varies exponentially with $T_{\rm eff}$, which gives 1.66 μHz, still in agreement with the observed value.

Fig. 9. Linewidths of $\ell = 0$ modes as a function of frequency. Same legend as in Fig. 8. A single linewidth was fitted for each order.

Fig. 10. Amplitude of $\ell = 0$ modes as a function of frequency. Same legend as in Fig. 8.

7.6. Amplitudes

From the heights and linewidths of the modes in the power spectrum, we can compute the rms amplitude of each mode according to the following expression:

$$A_{\ell,n} = \sqrt{\frac{\pi \Gamma_{\ell,n} H_{\ell,n}}{2}}, \qquad (6)$$

where $\Gamma_{\ell,n}$ is the width of the mode (ℓ, n) and $H_{\ell,n}$ is the height of that mode in a single-sided power spectrum (hence the factor 2 in the numerator). The values obtained are listed in Table 7 and are shown in Fig. 10. We can see the profile of the p-mode bump. The maximum mode amplitude is 3.82 ± 0.30 ppm, which agrees with the value obtained in Sect. 4.1 (3.61 ± 0.35 ppm). Owing to the imperfect observational window (with a duty cycle of ~0.83), there is a substantial leakage of mode power in small aliases. We corrected the amplitude for this effect, which led to an observed value of 4.12 ± 0.32 ppm. To take into account the response function of CoRoT, we converted the amplitude to the bolometric one by computing $R_{\text{osc}} = 7.87$ and $R_{\ell=0} = 4.44$ (see Michel et al. 2009, for details), which gives the bolometric correction $c_{\text{bol}} = 0.90 \pm 0.01$. Finally, since HD 169392 is a binary, a part of the observed total flux comes from the secondary component. With the magnitude quoted in Sect. 1, we find $L_A/L_B = 3.9$, which allows us to conclude that ~20% of the flux is dimmed by the second component. Therefore, the final value for the maximal amplitude of the modes is $A_{\text{max}}^{\text{obs}} = 4.45 \pm 0.34$ ppm.
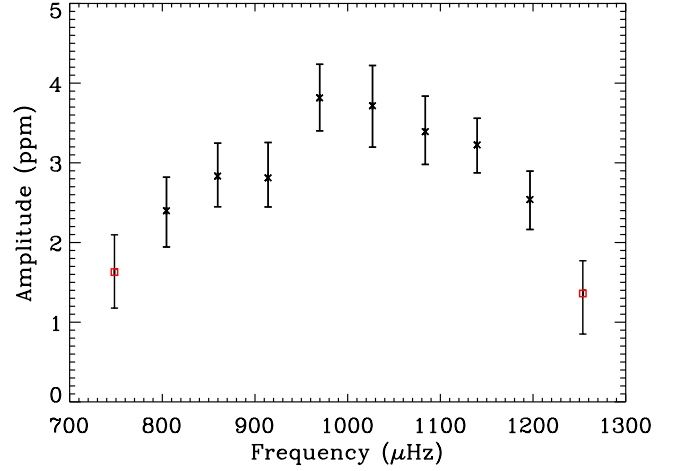
Several expressions have been developed the last few years to compute the maximum amplitude of the modes. According to Samadi et al. (2007b), the theoretical value of the maximum amplitude is obtained with

$$A_{\text{max}} = \left(\frac{L/L_\odot}{M/M_\odot}\right)^s \sqrt{\frac{5777}{T_{\text{eff}}}} A_{\odot,\text{max}}, \qquad (7)$$

with $s = 0.7$ and according to Michel et al. (2009), $A_{\odot,\text{max}} = 2.53 \pm 0.11$ ppm (in rms). Using the values of R and M from the AMP model (see Sect. 8), we obtain 6.02 ± 0.60 ppm.

We computed the theoretical value with the updated scaling relation derived by Kjeldsen & Bedding (2011), which depends on the lifetime of the modes, τ_{osc}:

$$A_{\text{max}} \propto \frac{L \tau_{\text{osc}}^{0.5}}{(M/M_\odot)^{1.5} T_{\text{eff}}^{2.25+r}}, \qquad (8)$$

We took $r = 1.5$ as adopted by Michel et al. (2008) and obtain 4.32 ± 1.10 ppm, which is much closer to the observed amplitude.

Huber et al. (2011) used several hundred red giants and main-sequence stars to derive an empirical relation, which is slightly different from the previous one but similar to the results obtained from red giants observed in clusters (Stello et al. 2011a). This relation is more dependent on the mass of the star:

$$A_{\text{max}} = \frac{(L/L_\odot)^s}{(M/M_\odot)^t} \frac{5777}{T_{\text{eff}}} A_{\odot,\text{max}}, \qquad (9)$$

with $s = 0.838$, $t = 1.32$, and $A_{\odot,\text{max}} = 2.53 \pm 0.11$ ppm (in rms), leading to 6.58 ± 0.79 ppm for Huber et al. (2011). Stello et al. (2011a) found slightly different parameters: $s = 0.95$ and $t = 1.8$ (in the adiabatic case), which gives $A_{\text{max}} = 7.21 \pm 0.92$ ppm.

The observed value is at the lower limit of the theoretical ones within 3-σ for modellings in Eqs. (7) and (9) and agrees within 1-σ with the prediction from Eq. (8).

7.7. Relative visibilities

Accurate estimation of the relative visibilities of non-radial modes is important for our knowledge of the physics of the stellar atmospheres because the visibilities depend on the stellar limb darkening and the observed wavelengths. Although well-defined in the Sun at different heights in the solar photosphere (Salabert et al. 2011), the measurements of relative visibilities are more critical for other stars due to lower S/N and shorter time series. Nevertheless, the mode visibilities were successfully determined in two of the CoRoT stars: HD 52265 (Ballot et al. 2011b) and HD 49385 (Deheuvels et al. 2010). The measured visibilities quantitatively agree well with theoretical calculations of limb-darkening functions from Ballot et al. (2011a), who also showed a dependence on T_{eff}.

Estimates of the relative visibilities, V_l^2, of $\ell = 1, 2$, and 3 modes were obtained for HD 169392A. Consistent values within the error bars were obtained among the different peak-fitting techniques. Some tests using different inclination angles and rotational splittings showed that the uncovered visibilities give similar results within the uncertainties. The relative visibility of the modes $\ell = 1, 2$, and 3 measured by the MCMC analysis are given in Table 8, as well as the median values of their distributions and associated 1-σ values.

Table 8. Medians and standard deviations for the inclination angle (i), the rotational splitting (ν_s), the projected splitting ($\nu_s \sin i$), and the relative visibilities of the $\ell = 1$, 2, and 3 modes ($V_{l=1}$, $V_{l=2}$, $V_{l=3}$) obtained from MCMC.

	i (°)	ν_s (μHz)	$\nu_s \sin i$ (μHz)	$V_{l=1}^2$	$V_{l=2}^2$	$V_{l=3}^2$
Median	36	0.62	0.38	1.41	0.68	0.15
$-\sigma$	20	0.23	0.16	0.17	0.11	0.07
$+\sigma$	36	0.59	0.11	0.20	0.11	0.08

Notes. These statistical informations are deduced from the joint-probability density function of the inclination/splitting and from the probability density function for the other parameters.

7.8. Splitting and inclination angle

We also checked the extent to which the estimated frequencies, amplitudes, and linewidths were independent of the assumed angle of inclination.

Multiple fits were performed for a fixed rotational splitting and a range of fixed angles, using the MCMC method. An additional check was performed by looking at the correlation map between width, inclination angle, and splittings from the MCMC technique. The mode frequencies returned by the various fits were found to be independent of the angle used, at the level of precision of the data. The mode linewidths and amplitudes showed a weak dependence on the angle of inclination and the splittings at extreme values of the inclination. But any changes were at a much lower level than the 1-σ error bars when the angle was in the range $15° \leq i \leq 85°$, i.e., the limits suggested by MCMC results.

Figure 11 shows the correlation map of the splitting and the inclination (two-dimensional probability density function). We notice two maxima of almost equally high probability into the joint-posterior probability density function. This bi-modality suggests that two different values for the joint-parameters are possible. However, the two solutions are compatible within 2σ and therefore are not statistically different (cf. Table 8). To achieve a more stringent determination, one would need additional constraints, such as the signature of the surface rotation, which unfortunately cannot be detected in the present dataset (see Sect. 5.2).

The product of the splitting and angle parameters, which gives the so-called projected splitting, $\nu_s \sin i$, is well-defined, as seen by the curved ridge and the uncertainties presented in Table 8. However, as anticipated by Ballot et al. (2006), a robust estimation of the individual parameters is hampered by two competing solutions, the first with relatively low angle and high splitting, and the second with high angle and lower splitting. Our inability to discern between the two solutions prevents us from reporting final values for each parameter.

8. Modelling HD 169392A

With the spectroscopic and asteroseismic information derived in the previous sections, we modelled HD 169392A using the Asteroseismic Modeling Portal (AMP, Metcalfe et al. 2009). This is a genetic algorithm that aims at optimising the match between the observed and the modelled frequencies of the star in addition to the spectroscopic constraints. The models are computed by the Aarhus STellar Evolution Code (Christensen-Dalsgaard 2008), which is also used to build the standard model of the Sun. It includes the OPAL 2005 equation of state (Rogers & Nayfonov 2002) and the most recent
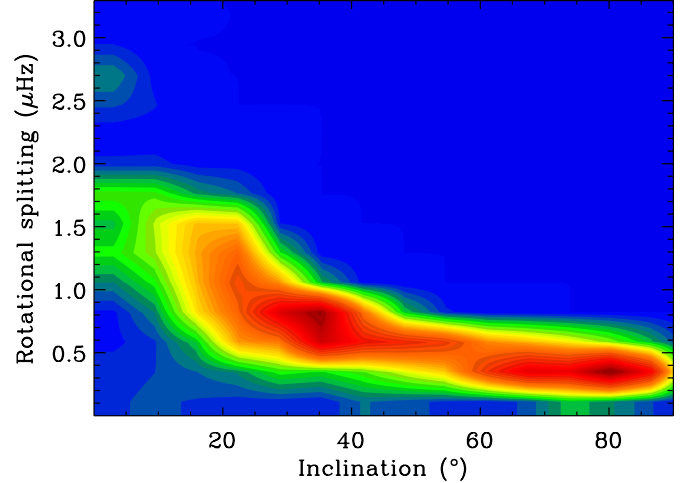
Fig. 11. Correlation map between rotational splitting and inclination. The red (yellow) region corresponds to the 1-σ (2-σ) confidence area.

OPAL opacities (Iglesias & Rogers 1996) associated with the low-temperature opacity table of Alexander & Ferguson (1994). Finally, the convection is treated according to the mixing-length theory (Böhm-Vitense 1958), and diffusion and gravitational settling of helium follow the prescription by Michaud & Proffitt (1993). A surface correction was applied to the frequencies following the prescription by Kjeldsen et al. (2008b). AMP has already modelled a large number of stars (e.g. Metcalfe et al. 2010; Mathur et al. 2012; Metcalfe et al. 2012) for a given physics.

For the observables, we used the spectroscopic constraints from Table 1 and the mode frequencies from the minimal list (Table 5). The best-fit model obtained has a χ^2 of 1.02. Since seismic and spectroscopic observables are used, we also computed two separate normalised χ^2: $\chi_{\rm spec}^2 = 0.22$ and $\chi_{\rm seis}^2 = 1.43$.

The $\chi_{\rm spec}^2$ agrees well for the observables and the best-fit model. In Fig. 6, the model frequencies are superimposed on the échelle diagram obtained with CoRoT data, and we can see that the best-fit model frequencies match the observations well. We also notice that the maximal list frequencies, including the $\ell = 3$ modes, are well-reproduced by the model, suggesting that these frequencies probably correspond to a real signal.

We obtained a mass of $M = 1.15 \pm 0.01\ M_\odot$, a radius of $R = 1.88 \pm 0.02\ R_\odot$, and an age $\tau = 4.33 \pm 0.12$ Gyr. The uncertainties come from estimated errors on the observables but do not include uncertainties in the surface layer correction, and the physics of stellar models.

Using the parallax $\pi = 13.82 \pm 1.2$ mas, we obtained a luminosity $L = 4.16 \pm 0.6\ L_\odot$ while the value from the best-fit model of AMP is $4.18 \pm 0.01\ L_\odot$, a very good agreement.

We also followed the methodology developed by Silva Aguirre et al. (2012) to couple the Casagrande et al. (2010) implementation of the infrared flux method (IRFM) with an asteroseismic analysis. This technique provides results using both the direct and grid-based methods, as well as a determination of the distance to the target. The results completely agree with those from the AMP analysis for $\log g$ and $T_{\rm eff}$ (see Table 9). The mass and radius agree with the first method to within 1σ and with the second one to within 2σ. The distance determined by these techniques is $d = 70 \pm 5.3$ pc, in excellent agreement with parallax measurements.

The best-fit model of AMP confirms that this is indeed a subgiant that has exhausted its central hydrogen and has no convective core. As seen on the HR diagram with the evolutionary track

Table 9. Modeling results from AMP, direct method + IRFM, and grid-based method + IRFM.

Method	M ($M_\odot$)	R ($R_\odot$)	τ (Gyr)	$\log g$ (dex)	$T_{\rm eff}$ (K)	$L/L_\odot$
AMP	1.15 ± 0.01	1.88 ± 0.02	4.33 ± 0.12	3.95 ± 0.01	6016 ± 5	4.18 ± 0.01
Direct method + IRFM	1.30 ± 0.23	1.93 ± 0.13	–	3.97 ± 0.02	6002 ± 77	4.45 ± 0.67
Grid-based method + IRFM	$1.25^{+0.05}_{-0.03}$	1.96 ± 0.02	–	3.95 ± 0.01	6002 ± 77	4.51 ± 1.04

Notes. The uncertainties for the AMP best fit model are the internal errors.
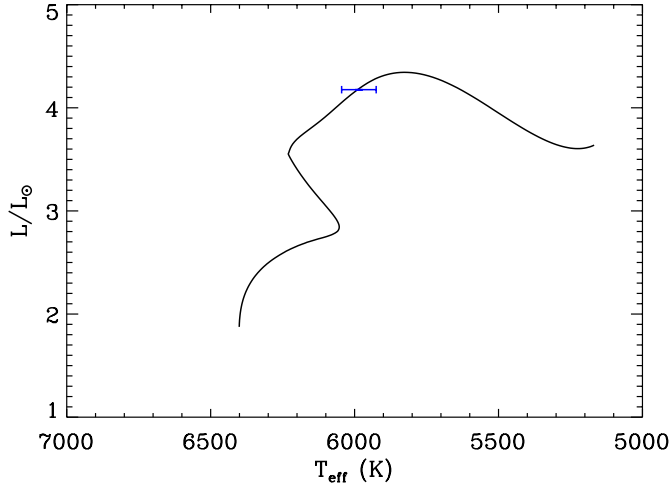
Fig. 12. Evolutionary track computed by AMP and position of the best-fit model with the spectroscopic uncertainty (blue symbol).

for this model (Fig. 12), it has not yet started to ascend the red giant branch.

9. Conclusion

In the present analysis we have derived the fundamental parameters of the two components of the binary system HD 169392 using HARPS observations. We obtained very close values of metallicity for the two components. This is quite similar to the results observed for other binary systems (e.g. 16 Cyg Metcalfe et al. 2012), suggesting that the A and B components were formed from the same cloud of gas and dust. Neither of the two components has significant amount of Li.

We were unable to detect a significant seismic signature of the B component from an analysis of the 91 days of CoRoT observations. This result agrees with the low detectability probability of 2% for the B component.

We determined the global parameters of the modes of HD 169392A, which led to $\langle \Delta \nu \rangle$ of 56.98 ± 0.05 μHz and $\nu_{\rm max}$ of 1030 ± 55 μHz, making this star very similar to another CoRoT target, HD 49385 (Deheuvels et al. 2010).

Nine groups reported p-mode parameters. The comparison of the results led to a minimal and maximal lists of frequencies. Some significant power was found in the region where we would expect $\ell = 3$ modes. We fitted the $\ell = 0$, 1, 2, and 3 modes together with the MCMC technique and obtained that three modes $\ell = 3$ are significant according to the a posteriori probability. We analysed the mixed modes of the star using their asymptotic properties and detected two avoided crossings at 816 μHz and 1336 μHz. From these avoided crossings, we derived the gravity spacing $\Delta \Pi_1 = 477 \pm 5$ s. We conclude that this star is quite evolved but not yet on the red-giant branch.

We derived the amplitude of the modes that is smaller than the predicted amplitudes within 1- to 3-σ depending on the theoretical formula applied. The linewidths of the modes obtained are consistent with the dependence on effective temperature derived by Appourchaux et al. (2012a) and Corsaro et al. (2012).

The study of the splittings and inclination angles led to two possible solutions. We obtained either an inclination angle of $20-40°$ with splittings of $0.4-1.0$ μHz, or an inclination angle of $55-85°$ and splittings of $0.2-0.5$ μHz. We note that no clear signature of the surface rotation was detected and in the absence of additional constraints, the significant correlation between the splitting and the inclination angle prevents us from constraining them more precisely.

The global parameters of the modes allowed us to give a first estimate of the mass and radius of the star using scaling relations based on solar values: 1.34 ± 0.26 $M_\odot$ and 1.97 ± 0.19 $R_\odot$. A more thorough modelling with AMP, based on the match of the individual mode frequencies and the spectroscopic parameters obtained in this work, provided $M = 1.15 \pm 0.01$ $M_\odot$, a radius of $R = 1.88 \pm 0.02$ $R_\odot$, and an age $\tau = 4.33 \pm 0.12$ Gyr.

References

Aizenman, M., Smeyers, P., & Weigert, A. 1977, A&A, 58, 41
Alexander, D. R., & Ferguson, J. W. 1994, ApJ, 437, 879
Anderson, E. R., Duvall, Jr., T. L., & Jefferies, S. M. 1990, ApJ, 364, 699
Appourchaux, T. 2008, Astron. Nachr., 329, 485
Appourchaux, T. 2011 [arXiv:1103.5352]
Appourchaux, T., Gizon, L., & Rabello-Soares, M.-C. 1998, A&AS, 132, 107
Appourchaux, T., Michel, E., Auvergne, M., et al. 2008, A&A, 488, 705
Appourchaux, T., Benomar, O., Gruberbauer, M., et al. 2012a, A&A, 537, A134
Appourchaux, T., Chaplin, W. J., García, R. A., et al. 2012b, A&A, 543, A54
Auvergne, M., Bodin, P., Boisnard, L., et al. 2009, A&A, 506, 411
Baglin, A., Auvergne, M., Boisnard, L., et al. 2006, in COSPAR, Plenary Meeting, 36th COSPAR Scientific Assembly, 36, 3749
Ballot, J., García, R. A., & Lambert, P. 2006, MNRAS, 369, 1281
Ballot, J., Barban, C., & van't Veer-Menneret, C. 2011a, A&A, 531, A124
Ballot, J., Gizon, L., Samadi, R., et al. 2011b, A&A, 530, A97

Barban, C., Deheuvels, S., Baudin, F., et al. 2009, A&A, 506, 51
Basu, S., Grundahl, F., Stello, D., et al. 2011, ApJ, 729, L10
Baudin, F., Barban, C., Belkacem, K., et al. 2011, A&A, 529, A84
Belkacem, K., Goupil, M. J., Dupret, M. A., et al. 2011, A&A, 530, A142
Belkacem, K., Dupret, M. A., Baudin, F., et al. 2012, A&A, 540, L7
Benomar, O. 2008, Commun. Asteroseismol., 157, 98
Benomar, O., Bedding, T. R., Stello, D., et al. 2012, ApJ, 745, L33
Böhm-Vitense, E. 1958, ZAp, 46, 108
Borucki, W. J., Koch, D., Basri, G., et al. 2010, Science, 327, 977
Brown, T. M., Gilliland, R. L., Noyes, R. W., & Ramsey, L. W. 1991, ApJ, 368, 599
Bruntt, H., Bedding, T. R., Quirion, P.-O., et al. 2010, MNRAS, 405, 1907
Bruntt, H., Basu, S., Smalley, B., et al. 2012, MNRAS, 423, 122
Campante, T. L., Handberg, R., Mathur, S., et al. 2011, A&A, 534, A6
Casagrande, L., Ramírez, I., Meléndez, J., Bessell, M., & Asplund, M. 2010, A&A, 512, A54
Catala, C., Poretti, E., Garrido, R., et al. 2006, in ESA SP 1306, eds. M. Fridlund, A. Baglin, J. Lochard, & L. Conroy, 329
Chaplin, W. J., Houdek, G., Karoff, C., Elsworth, Y., & New, R. 2009, A&A, 500, L21
Chaplin, W. J., Kjeldsen, H., Bedding, T. R., et al. 2011a, ApJ, 732, 54
Chaplin, W. J., Kjeldsen, H., Christensen-Dalsgaard, J., et al. 2011b, Science, 332, 213
Christensen-Dalsgaard, J. 2002, Rev. Mod. Phys., 74, 1073
Christensen-Dalsgaard, J. 2004, Sol. Phys., 220, 137
Christensen-Dalsgaard, J. 2008, Ap&SS, 316, 13
Christensen-Dalsgaard, J., & Thompson, M. J. 2011, in Astrophysical Dynamics: From Stars to Galaxies, Proc. of the International Astronomical Union, IAU Symp., 271, 32
Corsaro, E., Stello, D., Huber, D., et al. 2012, ApJ, 757, 190
Creevey, O. L., Doğan, G., Frasca, A., et al. 2012, A&A, 537, A111
Deheuvels, S., & Michel, E. 2011, A&A, 535, A91
Deheuvels, S., Bruntt, H., Michel, E., et al. 2010, A&A, 515, A87
Duncan, D. K. 1984, AJ, 89, 515
Escobar, M. E., Théado, S., Vauclair, S., et al. 2012, A&A, 543, A96
Fletcher, S. T., Broomhall, A.-M., Chaplin, W. J., et al. 2011, MNRAS, 413, 359
García, R. A., Régulo, C., Samadi, R., et al. 2009, A&A, 506, 41
García, R. A., Hekker, S., Stello, D., et al. 2011, MNRAS, 414, L6
Gaulme, P., Appourchaux, T., & Boumier, P. 2009, A&A, 506, 7
Gaulme, P., Vannier, M., Guillot, T., et al. 2010, A&A, 518, L153
Goldreich, P., & Keeley, D. A. 1977, ApJ, 212, 243
Gough, D. O., Kosovichev, A. G., Toomre, J., et al. 1996, Science, 272, 1296
Gould, B. A. 1855, AJ, 4, 81
Gustafsson, B., Edvardsson, B., Eriksson, K., et al. 2008, A&A, 486, 951
Handberg, R., & Campante, T. L. 2011, A&A, 527, A56
Harvey, J. 1985, in Future Missions in Solar, Heliospheric & Space Plasma Physics, eds. E. Rolfe, & B. Battrick, ESA SP, 235, 199
Hekker, S., Broomhall, A., Chaplin, W. J., et al. 2010a, MNRAS, 402, 2049
Hekker, S., Debosscher, J., Huber, D., et al. 2010b, ApJ, 713, L187
Hekker, S., Elsworth, Y., De Ridder, J., et al. 2011, A&A, 525, A131
Holmberg, J., Nordström, B., & Andersen, J. 2007, A&A, 475, 519
Howell, S. B., Rowe, J. F., Bryson, S. T., et al. 2012, ApJ, 746, 123
Huber, D., Bedding, T. R., Stello, D., et al. 2011, ApJ, 743, 143
Iglesias, C. A., & Rogers, F. J. 1996, ApJ, 464, 943
Israelian, G., Santos, N. C., Mayor, M., & Rebolo, R. 2004, A&A, 414, 601
Kjeldsen, H., & Bedding, T. R. 1995, A&A, 293, 87

Kjeldsen, H., & Bedding, T. R. 2011, A&A, 529, L8
Kjeldsen, H., Bedding, T. R., Arentoft, T., et al. 2008a, ApJ, 682, 1370
Kjeldsen, H., Bedding, T. R., & Christensen-Dalsgaard, J. 2008b, ApJ, 683, L175
Koch, D. G., Borucki, W. J., Basri, G., et al. 2010, ApJ, 713, L79
Kupka, F., Piskunov, N., Ryabchikova, T. A., Stempels, H. C., & Weiss, W. W. 1999, A&AS, 138, 119
Mathur, S., García, R. A., Catala, C., et al. 2010a, A&A, 518, A53
Mathur, S., García, R. A., Régulo, C., et al. 2010b, A&A, 511, A46
Mathur, S., Handberg, R., Campante, T. L., et al. 2011a, ApJ, 733, 95
Mathur, S., Hekker, S., Trampedach, R., et al. 2011b, ApJ, 741, 119
Mathur, S., Metcalfe, T. S., Woitaszek, M., et al. 2012, ApJ, 749, 152
Mayor, M., Pepe, F., Queloz, D., et al. 2003, The Messenger, 114, 20
Mazumdar, A., Michel, E., Antia, H. M., & Deheuvels, S. 2012, A&A, 540, A31
Metcalfe, T. S., Creevey, O. L., & Christensen-Dalsgaard, J. 2009, ApJ, 699, 373
Metcalfe, T. S., Monteiro, M. J. P. F. G., Thompson, M. J., et al. 2010, ApJ, 723, 1583
Metcalfe, T. S., Chaplin, W. J., Appourchaux, T., et al. 2012, ApJ, 748, L10
Michaud, G., & Proffitt, C. R. 1993, in Inside the Stars, eds. W. W. Weiss, & A. Baglin, IAU Colloq., 137, ASP Conf. Ser., 40, 246
Michel, E., Baglin, A., Auvergne, M., et al. 2008, Science, 322, 558
Michel, E., Samadi, R., Baudin, F., et al. 2009, A&A, 495, 979
Mosser, B., & Appourchaux, T. 2009, A&A, 508, 877
Mosser, B., Baudin, F., Lanza, A. F., et al. 2009a, A&A, 506, 245
Mosser, B., Michel, E., Appourchaux, T., et al. 2009b, A&A, 506, 33
Mosser, B., Goupil, M. J., Belkacem, K., et al. 2012, A&A, 540, A143
Nordström, B., Mayor, M., Andersen, J., et al. 2004, A&A, 418, 989
Osaki, J. 1975, PASJ, 27, 237
Peirce, B. 1852, AJ, 2, 161
Piau, L., Turck-Chièze, S., Duez, V., & Stein, R. F. 2009, A&A, 506, 175
Poretti, E., Rainer, M., Mantegazza, L., et al. 2012 [arXiv:1202.3542]
Press, W. H., Teukolsky, S. A., Vetterling, W. T., & Flannery, B. P. 1992, Numerical recipes in FORTRAN, The art of scientific computing, 2nd edn. (Cambridge: University Press)
Rainer, M. 2003, Ph.D. Thesis, Università degli Studi di Milano
Rogers, F. J., & Nayfonov, A. 2002, ApJ, 576, 1064
Roxburgh, I. W., & Vorontsov, S. V. 2003, A&A, 411, 215
Salabert, D., Fossat, E., Gelly, B., et al. 2004, A&A, 413, 1135
Salabert, D., Ballot, J., & García, R. A. 2011, A&A, 528, A25
Samadi, R. 2011, in The Pulsations of the Sun and the Stars, eds. J.-P. Rozelot, & C. Neiner (Berlin Springer Verlag), Lect. Notes Phys., 832
Samadi, R., Fialho, F., Costa, J. E. S., et al. 2007a [arXiv:astro-ph/0703354]
Samadi, R., Georgobiani, D., Trampedach, R., et al. 2007b, A&A, 463, 297
Sato, K. H., Garcia, R. A., Pires, S., et al. 2010, ArXiv e-prints 1003.5178
Silva Aguirre, V., Casagrande, L., Basu, S., et al. 2012, ApJ, 757, 99
Sinachopoulos, D., Gavras, P., Dionatos, O., Ducourant, C., & Medupe, T. 2007, A&A, 472, 1055
Stello, D., Huber, D., Kallinger, T., et al. 2011a, ApJ, 737, L10
Stello, D., Meibom, S., Gilliland, R. L., et al. 2011b, ApJ, 739, 13
Struve, O., Franklin, K., & Stableford, C. 1955, ApJ, 121, 670
Unno, W., Osaki, Y., Ando, H., Saio, H., & Shibahashi, H. 1989, Nonradial oscillations of stars
Uytterhoeven, K., Poretti, E., Rainer, M., et al. 2008, J. Phys. Conf. Ser., 118, 012077
van Leeuwen, F. 2007, A&A, 474, 653
Verner, G. A., Elsworth, Y., Chaplin, W. J., et al. 2011, MNRAS, 892
White, T. R., Bedding, T. R., Stello, D., et al. 2011, ApJ, 742, L3

Page 13 is available in the electronic edition of the journal at http://www.aanda.org

Table 5. Minimal and maximal lists of frequencies for HD 169392 in μHz obtained from 91 days of CoRoT observations with MCMC.

Order	$\ell = 0$	$\ell = 1$	$\ell = 2$	$\ell = 3$
12	...	...	743.22 ± 1.34^a	
13	748.35 ± 0.40^a	770.96 ± 0.37	797.97 ± 0.76	...
14	804.50 ± 0.35	838.21 ± 0.38	853.50 ± 0.85	...
15	859.70 ± 0.38	886.83 ± 0.23	909.34 ± 0.46	...
16	914.14 ± 0.27	940.52 ± 0.27	965.45 ± 0.41	930.52 ± 1.87^b
17	969.77 ± 0.46	996.40 ± 0.32	1022.18 ± 0.27	986.08 ± 1.20^b
18	1026.79 ± 0.27	1052.68 ± 0.20	1080.04 ± 0.44	1043.43 ± 1.23^b
19	1083.77 ± 0.39	1109.19 ± 0.36	1137.05 ± 0.58	...
20	1139.76 ± 0.42	1166.17 ± 0.34	1193.29 ± 0.97	...
21	1196.71 ± 0.73	1221.76 ± 1.38	1248.79 ± 1.44^a	...
22	1253.73 ± 0.75^a	...	...	...

Notes. $^{(a)}$ Modes that belong to the maximal list. $^{(b)}$ Significant modes according to the MCMC method.

Table 7. Amplitudes and linewidths for all modes of Table 5 computed with the MCMC.

l	n	Linewidth (μHz)	$+\sigma$	$-\sigma$	Amplitude (ppm)	$+\sigma$	$-\sigma$
0	13	0.80	1.02	0.64	1.63	0.33	0.32
0	14	1.39	0.65	0.62	2.40	0.30	0.32
0	15	1.35	0.39	0.30	2.83	0.29	0.27
0	16	1.30	0.63	0.43	2.81	0.31	0.26
0	17	2.37	0.61	0.52	3.82	0.30	0.29
0	18	1.00	0.57	0.27	3.72	0.36	0.37
0	19	2.01	0.77	0.54	3.39	0.31	0.29
0	20	1.97	0.58	0.47	3.23	0.24	0.25
0	21	4.14	1.53	1.18	2.54	0.25	0.27
0	22	1.27	1.35	0.77	1.36	0.29	0.36
1	13	0.80	1.02	0.64	1.94	0.38	0.40
1	14	1.39	0.65	0.62	2.84	0.37	0.37
1	15	1.35	0.39	0.30	3.37	0.32	0.31
1	16	1.30	0.63	0.43	3.35	0.34	0.32
1	17	2.37	0.61	0.52	4.53	0.34	0.33
1	18	1.00	0.57	0.27	4.40	0.42	0.38
1	19	2.01	0.77	0.54	4.04	0.33	0.33
1	20	1.97	0.58	0.47	3.83	0.31	0.31
1	21	4.14	1.53	1.18	3.02	0.31	0.33
2	12	0.80	1.02	0.64	1.34	0.28	0.27
2	13	1.39	0.65	0.62	1.96	0.28	0.27
2	14	1.35	0.39	0.30	2.33	0.25	0.24
2	15	1.30	0.63	0.43	2.32	0.25	0.23
2	16	2.37	0.61	0.52	3.13	0.25	0.25
2	17	1.00	0.57	0.27	3.04	0.32	0.29
2	18	2.01	0.77	0.54	2.79	0.26	0.26
2	19	1.97	0.58	0.47	2.64	0.27	0.24
2	20	4.14	1.53	1.18	2.08	0.23	0.25
2	22	1.69	1.42	0.91	0.99	0.27	0.29
3	16	1.30	0.63	0.43	0.65	0.07	0.06
3	17	2.37	0.61	0.52	0.89	0.07	0.07
3	18	1.00	0.57	0.27	0.86	0.08	0.09